VSP

Advanced Robotics 23 (2009) 1327–1358

ADVANCED ROBOTICS
www.brill.nl/ar

Full paper

iSoRA: Humanoid Robot Arm for Intelligent Haptic Interaction with the Environment

Dzmitry Tsetserukou *, **Naoki Kawakami and Susumu Tachi**

Department of Information Physics and Computing, University of Tokyo, 7-3-1 Hongo, Bunkyo-ku, Tokyo 113-8656, Japan

Received 5 November 2008; accepted 7 February 2009

Abstract

The paper concentrates on the development and control of the humanoid robot arm iSoRA, intended for operation in a dynamic unstructured environment. Optical torque sensors integrated into each joint enable measurement of contacting forces along the entire manipulator surface. A variable admittance control strategy was elaborated to increase the robot functionality and to achieve the human-like dynamics of interaction. The experimental results show that the proposed approach not only provides safe interaction of the robot arm with a person, but also improves the effectiveness of contact task performance. The paper also presents a novel concept of avoidance of an obstacle of unknown shape. The tactile sensory ability of the developed manipulator allows robot links to follow the object contour and to perform motion planning in the dynamic environment. The information on the applied normal force vector, object shape and target point coordinates is supplied to the motion planning system. The algorithms for contact point detection, object geometry recognition, and estimation of contacting object stiffness are detailed. The numerical simulation elicits a capability of the proposed method to approximate various object shapes precisely. The experimental results showed that the local admittance control and motion planner allowed the end-effector to follow the object contour in a very smooth, consistent manner while reaching the target point.

Keywords

Humanoid robot arm, variable admittance control, human–robot interaction, obstacle avoidance, optical torque sensor

1. Introduction

Service robotics aimed at assisting humans in everyday life environments is nowadays gaining increased interest from researchers and industry. Such robots are programmed to perform continuously changing tasks in unstructured human envi-

* To whom correspondence should be addressed. E-mail: dima_teterukov@ipc.i.u-tokyo.ac.jp

 DOI:10.1163/156855309X462619

ronments. Both coexistence, when the human and robot share the same workspace, and cooperation, when the human and robot work on the same task, impose strict requirements on manipulator behavior and control in order to ensure safe interaction with the environment, effectiveness of target task execution and ergonomic cooperation.

Classical motion planning algorithms for general manipulators in cluttered environments first construct the robot configuration space with a known set of stationary obstacles and then generate collision-free motions in the configuration space [1]. In the case of real indoor environments, known obstacles (e.g., chairs, tables, etc.) and unknown obstacles (persons approaching the robot, unmapped environment, etc.) change their location dynamically. Moreover, the object shape, speed and position can also alter in an unpredictable way, leading to obstruction of the planned robot motion.

Thus, the robot control system faces three main issues: (1) establishing safe physical contact with environment, (2) planning collision-free motion and recognition of obstacle shapes, and (3) directing the robot to its goal position. To meet these challenges, sensor-based planning making use of real-time sensor information about the surroundings is needed.

For an autonomous mobile robot moving in an unknown environment, non-tactile sensors are normally used. A variety of algorithms for shape recognition from camera images has been developed (e.g., stereo vision, optical flow). However, these techniques usually require a lot of computation and, therefore, are not suitable for real-time use [2].

When it comes to a multi-d.o.f. robot manipulator working in an unknown environment, the issues of obstacle avoidance become much more complicated because of the high risk of collision of each joint and each link of the robot arm with an obstacle. The most effective solution for preventing collisions is to endow the whole robot arm with the ability to safely contact and interact with environment in real-time. Lumelsky [3] pioneered the idea to cover a manipulator with a sensitive skin capable of detecting nearby objects. An array of infrared proximity sensors delivers the information about any obstacles obstructing the arm motion to the control system. The algorithm of the motion planner maneuvers the robot arm, thus avoiding contact [4, 5]. Recently, a high-speed vision system attached to the robot manipulator for collision avoidance was developed [6].

We argue that the robot arm should be controlled not to avoid physical contact, but rather to ensure safe tactile interaction with the environment during obstacle avoidance. The benefits of such interaction are obvious. The robot can acquire plenty of fundamental information about objects by touch (shape, stiffness, texture, location, fixation, etc.) and plan its motion in the most optimal fashion. It should be noted that tasks under human supervision, such as transporting the object, leading the robot tip *via* force-following and performing the assembling tasks, require the processing algorithm of the contact state. Conventional approaches to handle the physical interaction between a manipulator and environment are based

on the impedance control of a robot arm tip [7]. However, the other parts of the robot body (forearm, elbow, upper arm, shoulder and torso) are insensitive to contact and present significant danger not only to humans, but also to the robot structure itself. Generally, two techniques of safe interaction with the entire robot arm are well recognized, i.e., passive compliance control and active force control.

Whereas mechanical leaf springs [8] and variable stiffness actuators [9] integrated into each joint allow achieving a fast response to an external disturbance, they also cause vibrations destabilizing the dynamic behavior. Additionally, the robot control in such cases is complicated by many unknown parameters (e.g., actuator stiffness and damping). Another approach to improve the intrinsic safety of the robot is to reduce the weight of components. The main drawback of this method is the occurrence of undamped structural vibrations.

Active force control implies that the robot structure is stiff enough to provide high position accuracy and contact ability with environment is achieved by excessive sensory system feedback [10]. However, due to the time lag induced by the sampling process, such robots pose dangers at the moment of impact. Mitsunaga *et al.* [11] progressively improved the tactile ability of the robot through covering its entire body with piezoelectric film-based tactile sensors. Since this device integrates a huge amount of small sensors incorporated into soft layer, and requires complicated wiring and signal processing hardware, it has high cost and reliability issues.

2. Robot Arm and Sensory System

To realize the safe physical contact of the entire robot arm structure with humans and to guarantee obstacle avoidance, we developed a whole-sensitive robot arm iSoRA (*i*ntelligent *So*ft *R*obot *A*rm) (by using distributed torque sensors in each joint). When contact with the environment occurs, the manipulator automatically generates compliant motion according to the measured external force (active control). Thus, the whole structure of the manipulator can safely interact with an unstructured environment. The torque sensors introduce compliances, which soften the impact forces on the initial state of the contact transient (passive control).

The developed robot arm iSoRA (Fig. 1) has 4 d.o.f.: roll, pitch and yaw joints of a shoulder, and a pitch joint of an elbow. Such orthogonal disposition of the axes simplifies the installation of the torque sensors and motor drives into the joints. Coordinate systems based on the Denavit–Hartenberg convention are represented in Fig. 2. The 8-d.o.f. robot hand allows performing dexterous manipulations.

Each robot joint is equipped with an optical torque sensor. The sizes and appearance of the arm were chosen so that any sense of incongruity during interaction with a human is avoided. We kept the arm proportions the same as in an average height human, aged 25: upper arm length L_1 0.308 m, upper arm circumference 0.251 m, forearm length L_2 0.241 m and forearm circumference 0.189 m.

The specific application (i.e., a robot arm interacting with human beings in a safe manner) introduces special requirements for the design of the torque sensor.

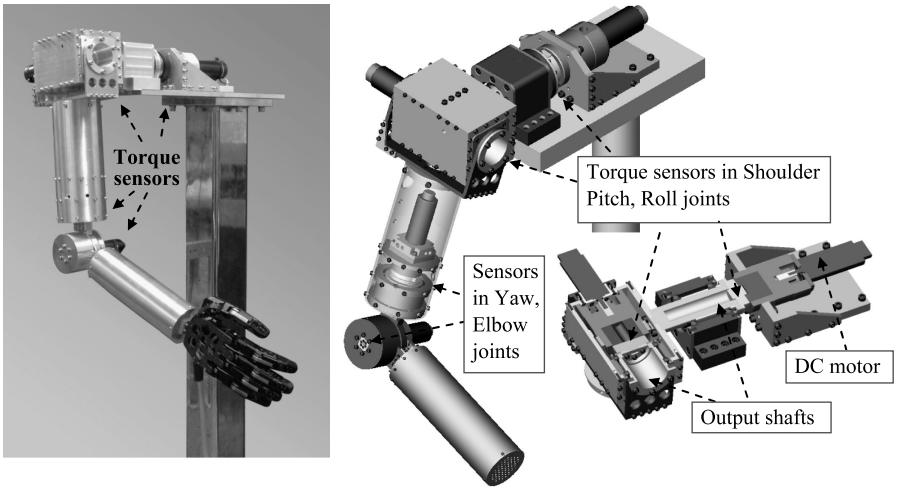

Figure 1. Robot arm iSoRA.

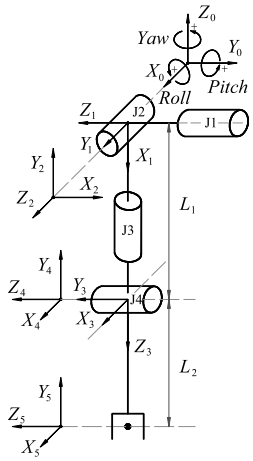

Figure 2. Coordinate system.

In order to facilitate the realization of torque measurement in each arm joint, we developed new optical torque sensors based on results presented in Refs [12, 13]. The novelty of our method is the application of the ultra-small-size photointerrupter (PI) RPI-121 as a sensitive element to measure the relative motion of sensor components. The dimensions of the PI (3.6 mm × 2.6 mm × 3.3 mm) and its weight of 0.05 g allow realization of a compact design. The spring components were manufactured from one piece of AISI 4135 steel using a wire electrical discharge machining. The optical torque sensor is set between the driving shaft of the harmonic transmission and driven shaft of the joint (Fig. 3). When the load is applied to the robot joint, the magnitude of the output signal from PI corresponds to the exerted load.

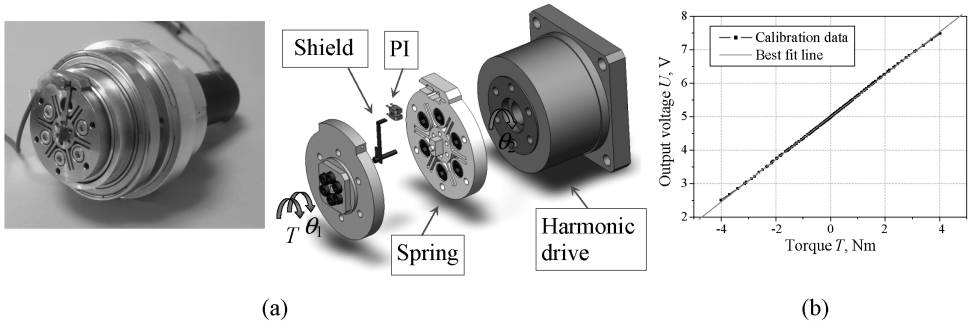

Figure 3. Torque sensor of the elbow joint and calibration results. (a) Optical torque sensor. (b) Calibration results.

The sensors attached to the first, second and third/fourth joints were designed to measure torques of ±12.5, ±10.5 and ±4.5 Nm, respectively. A non-linearity of 2.5% FS was calculated using the maximum deviated value from the best-fit line. The developed optical torque sensors are characterized by high dependability, good accuracy (even in electrically noisy environments), low price, compact size, light weight, and easy mounting procedure.

3. Intelligent Variable Admittance Control

3.1. Joint Impedance Control

The dynamic equation of an n-d.o.f. manipulator in joint space coordinates (during interaction with the environment) is given by:

$$M(\theta)\ddot{\theta} + C(\theta, \dot{\theta})\dot{\theta} + \tau_{\mathrm{f}}(\dot{\theta}) + G(\theta) = \tau + \tau_{\mathrm{EXT}}, \tag{1}$$

where θ, $\dot{\theta}$ and $\ddot{\theta}$ are the joint angle, the joint angular velocity and the joint angle acceleration, respectively, $M(\theta) \in R^{n\times n}$ is the symmetric positive definite inertia matrix, $C(\theta, \dot{\theta}) \in R^n$ is the vector of Coriolis and centrifugal torques, $\tau_{\mathrm{f}}(\dot{\theta}) \in R^n$ is the vector of actuator joint friction torques, $G(\theta) \in R^n$ is the vector of gravitational torques, $\tau \in R^n$ is the vector of actuator joint torques, and $\tau_{\mathrm{EXT}} \in R^n$ is the vector of external disturbance joint torques.

People can perform dexterous contact tasks in daily activities, regulating their own dynamics according to a time-varying environment. To achieve skillful human-like behavior, the humanoid robot has to be able to change its dynamic characteristics depending on time-varying interaction forces. The most efficient method of controlling the interaction between a manipulator and an environment is impedance control [14]. This approach enables us to regulate response properties of the robot to external forces through modifying the mechanical impedance parameters. A schematic representation of joint impedance control is given in Fig. 4.

The desired impedance properties of the ith joint of manipulator can be expressed as:

$$J_{\mathrm{d}i}\,\Delta\ddot{\theta}_i + D_{\mathrm{d}i}\,\Delta\dot{\theta}_i + K_{\mathrm{d}i}\,\Delta\theta_i = \tau_{\mathrm{EXT}i}; \qquad \Delta\theta_i = \theta_{\mathrm{c}i} - \theta_{\mathrm{d}i}, \tag{2}$$

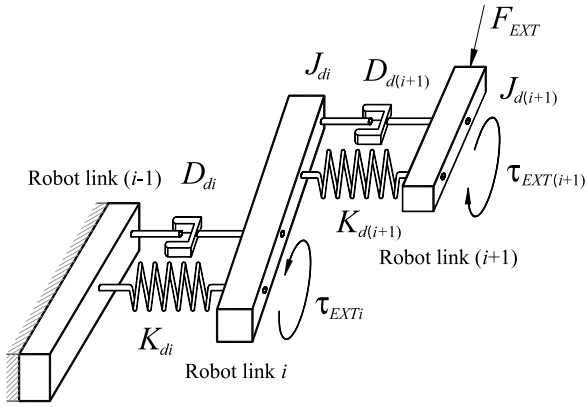

Figure 4. Concept of the local impedance control: when external force F_{EXT} is applied to the robot link $i+1$, assigned values of desired inertia $J_{\mathrm{d}(i+1)}$, damping $D_{\mathrm{d}(i+1)}$ and stiffness $K_{\mathrm{d}(i+1)}$ of the $i+1$ joint define the dynamic properties of this robot joint in response to the exerted external torque $\tau_{\mathrm{EXT}(i+1)}$.

where $J_{\mathrm{d}i}$, $D_{\mathrm{d}i}$ and $K_{\mathrm{d}i}$ are the desired inertia, damping and stiffness of the ith joint, respectively, $\tau_{\mathrm{EXT}i}$ is the torque applied to ith joint and caused by external forces, and $\Delta\theta_i$ is the difference between the current position $\theta_{\mathrm{c}i}$ and desired position $\theta_{\mathrm{d}i}$. The state-space presentation of the equation of local impedance control is written as:

$$\begin{bmatrix} \Delta\dot{\theta}_i \\ \dot{v}_i \end{bmatrix} = \begin{bmatrix} 0 & 1 \\ -K_{\mathrm{d}i}/J_{\mathrm{d}i} & -D_{\mathrm{d}i}/J_{\mathrm{d}i} \end{bmatrix} \begin{bmatrix} \theta_i \\ v_i \end{bmatrix} + \begin{bmatrix} 0 \\ 1/J_{\mathrm{d}i} \end{bmatrix} \tau_{\mathrm{EXT}i}(t), \tag{3}$$

or:

$$\begin{bmatrix} \Delta\dot{\theta}_i \\ \dot{v}_i \end{bmatrix} = A \begin{bmatrix} \theta_i \\ v_i \end{bmatrix} + B\,\tau_{\mathrm{EXT}i}(t), \tag{4}$$

where the state variable is defined as $v_i = \Delta\dot{\theta}_i$, and A and B are matrices. After integration of (4), the discrete time presentation of the impedance equation is expressed as:

$$\begin{bmatrix} \Delta\theta_{k+1} \\ \Delta\dot{\theta}_{k+1} \end{bmatrix} = A_{\mathrm{d}} \begin{bmatrix} \Delta\theta_k \\ \Delta\dot{\theta}_k \end{bmatrix} + B_{\mathrm{d}} T_{\mathrm{EXT}(k)}. \tag{5}$$

To achieve the fastest possible non-oscillatory response to the external force, we assigned the eigenvalues λ_1 and λ_2 of matrix A as real and equal to $\lambda_1 = \lambda_2 = \lambda$, $\lambda > 0$. By using the Cayley–Hamilton method for matrix exponential determination, we have:

$$A_{\mathrm{d}} = \mathrm{e}^{\lambda T} \begin{bmatrix} 1-\lambda T & T \\ -K_{\mathrm{d}}T/J_{\mathrm{d}} & 1-\lambda T - D_{\mathrm{d}}T/J_{\mathrm{d}} \end{bmatrix}, \tag{6}$$

$$B_{\mathrm{d}} = (A_{\mathrm{d}} - I)A^{-1}B = -\frac{1}{K_{\mathrm{d}}} \begin{bmatrix} \mathrm{e}^{\lambda T}(1-\lambda T) - 1 \\ -(D_{\mathrm{d}}/(2J_{\mathrm{d}}))^2 T \mathrm{e}^{\lambda T} \end{bmatrix}, \tag{7}$$

where T is the sampling time and I is the identity matrix.

There are several conflicting requirements on the choice of dynamics parameters of the impedance model to provide effectiveness and functionality of a service robot in tasks of physical interactions fulfilled in cooperation with humans and to ensure the collision avoidance. For example, while accomplishing service tasks for humans in the autonomous mode, it is required to provide high stiffness (to ensure small position error during object handling) and high damping (for good velocity tracking). Realization of human-following motion, mainly used in performing cooperative tasks, also imposes specific requirements on the desired impedance parameter selection. In this approach, by applying force to the robot arm, it is possible to intuitively operate the humanoid robot motion along the force and speed direction without considering any command signals. In the case of a collision, the very small stiffness is obligatory to reduce the impact forces.

Basically, there are two types of solution of this problem: adaptive and functional adjustments of impedance parameters. In adaptive control, the damping and stiffness of the system are gradually adjusted according to sensed dynamics and contact forces [15]. However, due to parametric uncertainties of the robot dynamics model, it is difficult to obtain the complete description of the dynamics. Therefore, model-based adaptive impedance control must rely on either repeated motions or time for adaptation to achieve convergence to the desired system parameters. For systems with more than 1 d.o.f., such an approach can hardly be applied. In the functional approaches, current impedance parameters have predetermined relations to the current sensed variables. Generally, these methods presume determining the current stiffness and damping matrices functionally dependent on sensed variables. The main idea of Ref. [16] is that the contact between the slave robot and the environment can be classified according to the angle between the commanded velocity and the contact force. It is supposed that force and velocity vectors are usually parallel when the impact occurs or when the object is being pushed. Thus, the functional dependency of stiffness and damping on the angle between sensed force and velocity vectors was proposed. In real cooperation tasks and, especially, collisions, these vectors can not only be parallel, but also have independent arbitrary directions according to the direction of the external force.

Another line of variable impedance research is directed to the estimation of human arm stiffness [17]. The proposed variable impedance controller varies a damping parameter of target impedance in proportion to an estimated value of the human arm stiffness. Despite the fact that humanoid robot arm can effectively follow the human arm motion, it cannot perform tasks autonomously. Besides, only impedance parameters of the robot end-effector can be adjusted. We elaborated a new methodology for impedance parameter adjustment based on the physical interaction mode and providing the dynamic stability of the system.

3.2. Intelligent Variable Joint Admittance Control

It was found that humans adjust their joint stiffness to accommodate changes in surface stiffness [18]. Furthermore, the research on impedance characteristics of a

human arm shows that, while pushing or pulling the object naturally, the human arm stiffness and damping behavior can be approximated by exponential curves [19]. The first essential peculiarity of the new control method is that we introduce the exponential functional dependency between the sensed force and stiffness to impart the human-like damping and stiffness behavior to the robot arm interacting with the environment. The second main feature originates from the fundamental conflict in impedance selection with regard to current working conditions. We consider the threshold of the external disturbance torque value $\tau_{\mathrm{EXT}th}$ to distinguish the service task (with high stiffness and damping of joints) from human-following motion tasks requiring low stiffness. This value can be chosen depending on the force necessary to accomplish the service task (e.g., lifting a box and physically supporting a disabled human require individual values of forces generated by the robot arm). We assigned the specific magnitude of $\tau_{\mathrm{EXT}th}$ to each joint of the robot arm. The third distinctive contribution is the recognition of the collision based on the time derivative of the joint torque.

3.2.1. Control for Accomplishment of Service Tasks and Human-Following Motion The procedure of impedance parameters selection is illustrated by the example of the elbow joint as follows. In the first stage, the parameters of desirable impedance model of the robot are computed for the case of service task accomplishment and the average level of contact force of the human–robot interaction. The desired stiffness K_{d1} (for the static equilibrium case) is calculated from (8) based on the maximum deflection value of the joint angle $\Delta\theta_{\max}$ caused by external torque τ_{EXT} while performing the service task:

$$K_{\mathrm{d1}} = \frac{\tau_{\mathrm{EXT}}}{\Delta\theta_{\max}}. \tag{8}$$

It was defined that a external torque of 1 Nm results in $\Delta\theta_{\mathrm{i}\max}$ of 0.1 rad giving K_{d1} of 10 (Nm/rad). The desired damping is expressed as:

$$D_{\mathrm{d1}} = 2\zeta\sqrt{K_{\mathrm{d1}} J_{\mathrm{d1}}}. \tag{9}$$

To realize a fast non-oscillatory response on the external torque, we defined the damping coefficient ζ as 1.05. The value of desired inertia J_{d1} of 0.1 (kg·m^2) was assigned to realize fast response tracking. Thus, the value D_{d1} of 2.1 (Nm·s/rad) was derived from (9). These parameters are valid till the interaction force does not cause any overload of robot arm. When the sensed value of the torque is higher than the threshold level, the robot recognizes this condition as the human-following motion mode and adjusts its dynamics parameters (stiffness and damping) in the same way as a human in order to provide smooth natural interaction. To realize such continuous change of dynamics, we use an exponential relation between the external disturbance torque and desired stiffness:

$$K_{\mathrm{d2}} = K_{\mathrm{d1}} \mathrm{e}^{\mu(\tau_{\mathrm{EXT}} - \tau_{\mathrm{EXT}th})}, \tag{10}$$

where K_{d2} is the desired stiffness on the second stage of the interaction, and μ is the coefficient defining the level of decreasing the arm joint stiffness in response to increasing the difference between external torque and torque threshold.

The desired damping is adjusted to prevent force responses from being too sluggish while changing stiffness values and to ensure contact stability:

$$D_{d2} = 2.1\sqrt{K_{d2} J_{d1}} = 2.1 e^{0.5\mu(\tau_{EXT} - \tau_{EXTth})} \sqrt{K_{d1} J_{d1}}. \quad (11)$$

Then, the variable joint impedance controller is described by:

$$J_{di} \Delta\ddot{\theta}_i + 2.1 e^{0.5\mu(\tau_{EXTi} - \tau_{EXTth})} \sqrt{K_{d1} J_{d1}} \Delta\dot{\theta}_i + K_{d1} e^{\mu(\tau_{EXTi} - \tau_{EXTth})} \Delta\theta_i = \tau_{EXTi};\ \Delta\theta_i = \theta_{ci} - \theta_{di}. \quad (12)$$

To verify the theory and to evaluate the feasibility and performance of the proposed impedance controller, experiments with the iSoRA robot arm were conducted. To ensure the effectiveness of service task accomplishment, we decided to implement position-based impedance control (admittance control) (Fig. 5, K_p, K_v, T_G and T_Z denote proportional gain, derivative gain of PD controller, torque caused by gravity forces, and torque measured by torque sensor, respectively). In this algorithm, the compliant trajectory generated by the impedance controller is tracked by the PD control loop.

During the experiment, the interaction with arm was performed to exceed the joint torque threshold level (τ_{EXTth} of 0.6 Nm was assigned, $\mu = -1.155$). The experimental results for the elbow joint — applied torque, impedance trajectories with constant (conventional approach) and variable coefficients (proposed intelligent variable joint admittance control), variable stiffness plot, variable damping

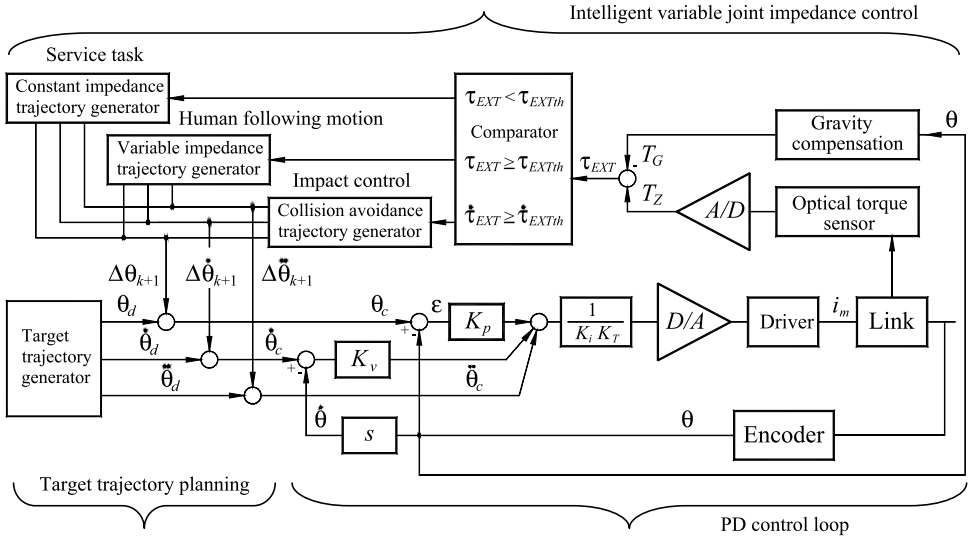

Figure 5. Block diagram of intelligent variable admittance control.

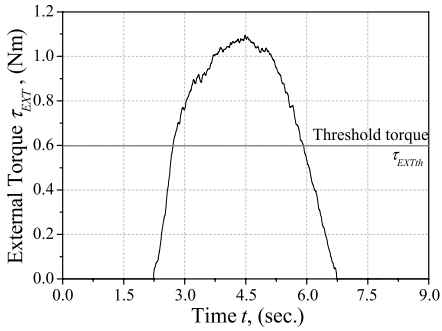

Figure 6. External torque.

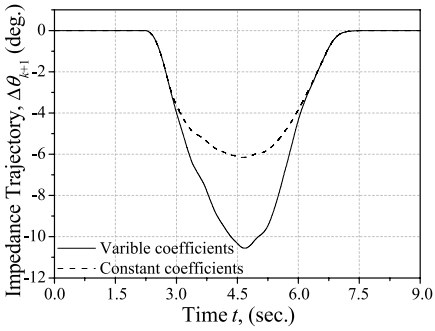

Figure 7. Impedance trajectories.

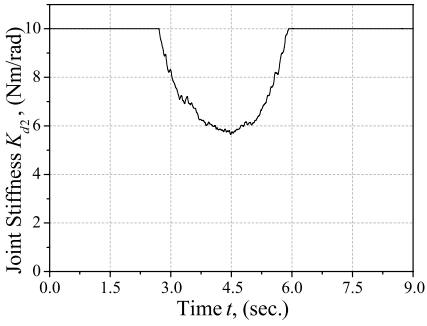

Figure 8. Variable stiffness $K_{\mathrm{d}2}$.

plot, applied torque with different magnitudes and corresponding impedance trajectories with constant and variable coefficients — are presented in Figs 6–11, respectively.

The experimental results show the successful realization of the variable joint impedance control. While contacting with the human, the robot arm generates compliant soft motion according to the sensed force. The plot presented in Fig. 7 shows that the variable impedance control provides a softer trajectory to accomplish the

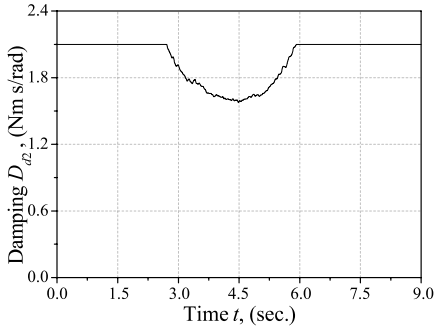

Figure 9. Variable damping D_{d2}.

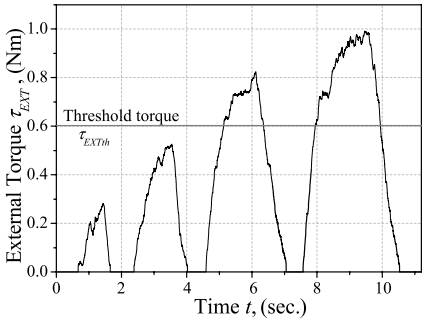

Figure 10. External torque.

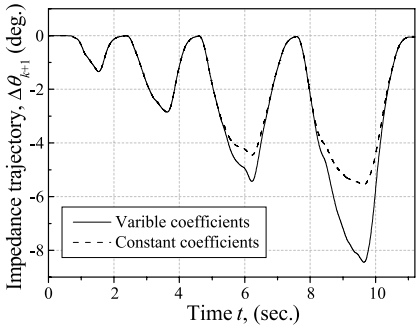

Figure 11. Impedance trajectories.

human-following motion than the impedance control with constant coefficients. As we assigned the critically damped response of the impedance model to the disturbance force, the output angle ($\Delta\theta_{k+1}$) has an ascending–descending exponential trajectory. As seen from the experimental results shown in Figs 10 and 11, the proposed variable impedance control comprehensively distinguishes and processes the service tasks (torques under threshold level) and cooperative human-following tasks (torques above threshold level). As the result of the experiments with the vari-

able impedance-controlled arm, tactile sensation of soft friendly interaction was achieved.

3.2.2. Intelligent Impact Control

In daily life, a person frequently contacts with an environment. The impact between a limb and the environment is inevitable during the interaction. In order to work in human daily environments, the service robot has to recognize the collision conditions, and its control system should be able to guide the manipulator quickly and smoothly so to avoid excessively large impact forces. Different impact control algorithms have been proposed. Basically, they focus on preparing for an impact in advance [20] and coping with impact during contact transience [21]. However, due to the unexpected nature of collisions and the lack of a robust control strategy of impact effect minimization, the application area of such approaches is greatly limited.

We believe that realization of robust impact control should originate from the human reflex system. A reflex action is an automatic involuntary neuromuscular action elicited by a defined stimulus and it can respond to external stimuli with a small reaction time retracting the limbs away from the object. In our control algorithm, impact is processed as follows. When an unexpected collision is detected, the impact control algorithm provides the pre-programmed reflex action of the robot arm. After accomplishing a safe and smooth collision, the control system is returned to the original mode aimed at distinguishing the service and cooperative tasks.

While analyzing the results of collision experiments, we came to conclusion that the large contact forces, mainly used as the criteria of collisions, do not indicate the impact, while the time derivative of the force value does. In the developed impact control system, the value of the time derivative of torque $\dot{\tau}_{\mathrm{EXT}th}$ exceeding the assigned threshold is interpreted as a collision state. To realize reflexive human-like behavior, the stiffness of the impedance model of the robot arm in the first stage of contact transient has to be reduced drastically. Hence, an exponential relation between the time derivative of the external torque and the desired stiffness coefficient $K_{\mathrm{d}3}$ was defined with a large coefficient μ of 0.7:

$$K_{\mathrm{d}3} = K_{\mathrm{d}1} \mathrm{e}^{-\mu \dot{\tau}_{\mathrm{EXT}th}}. \tag{13}$$

To attenuate the oscillations of the robot arm, which are inherent in collisions, the larger constant damping coefficient ζ of 1.25 was assigned. The value of the desired damping coefficient is calculated from (9). In the second stage of the contact transient, while the time derivative of torque is negative, a high damping value reducing arm inertia effect is desired. For this case, the following relation between desired damping $D_{\mathrm{d}3}$ and time derivative of torque was specified:

$$D_{\mathrm{d}3} = 2.5\sqrt{K_{\mathrm{d}1} J_{\mathrm{d}1}} - \alpha_{\mathrm{d}} \dot{\tau}, \tag{14}$$

where α_{d} is the weighting factor for damping (equal to 1.2).

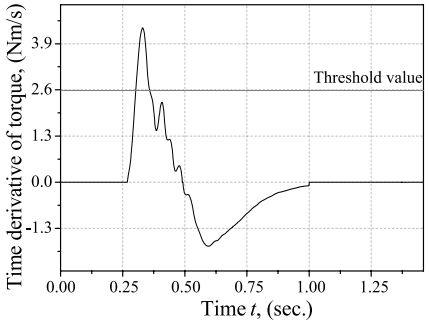

Figure 12. Torque derivation.

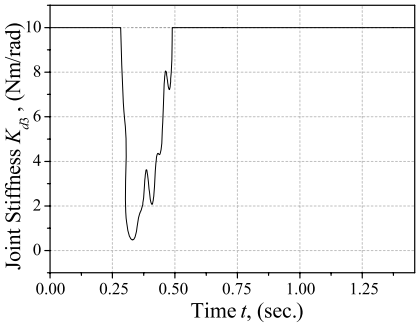

Figure 13. Variable stiffness K_{d3}.

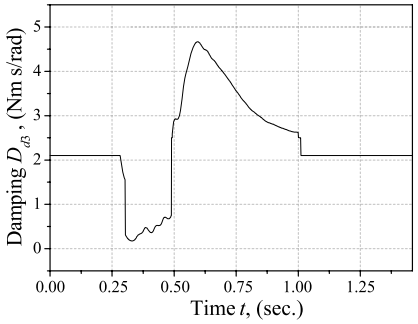

Figure 14. Variable damping D_{d3}.

The threshold value of the time derivative of torque $\dot{\tau}_{\mathrm{EXT}th}$ was 2.6 Nm/s. The experimental results for the elbow joint — time derivative of applied torque, desired collision stiffness K_{d3}, desired collision damping D_{d3} plot, impedance trajectories with constant and collision variable coefficients, time derivative of torque for two different contact states and corresponding impedance trajectories — are presented in Figs 12–17, respectively.

From the plots of experimental results, it is apparent that, when the impact is recognized (the time derivative of torque becomes larger than the threshold value),

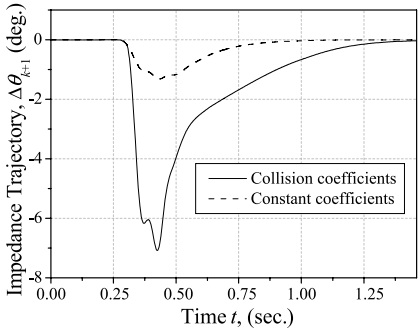

Figure 15. Impedance trajectories.

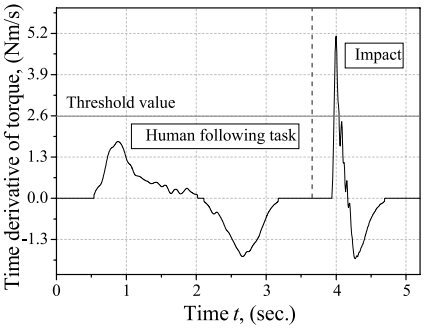

Figure 16. Torque derivation.

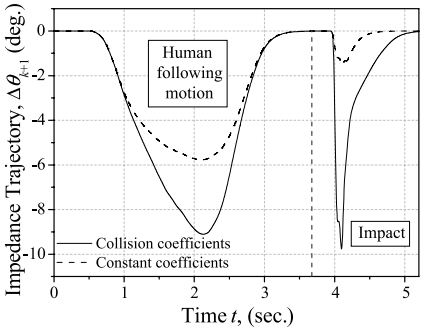

Figure 17. Impedance trajectories.

the stiffness and damping are decreasing drastically (Figs 13 and 14), allowing avoidance of large impact forces. In the second stage of the interaction, when the impact force is decreasing, the damping coefficient of the impedance model (Fig. 14) is increased to suppress the dynamic oscillations. Figure 16 indicates that the nature of cooperation tasks (graph of the time derivative of torque has a small value of local extremum and stretched in time-scale function) completely differs from the impact state (graph of the time derivative of torque has a large spike and

contracted in time-scale function). The developed control takes advantage of this feature to generate reflex action-based motion.

4. Novel Concept of Obstacle Avoidance and Object Exploration Through Tactile Interaction

4.1. Introduction and Problem Statement

Avoidance of an obstacle with an unknown shape in an unstructured environment is the fundamental and significant problem in service robotics, which has not yet been solved in a satisfactory way.

A fairly small amount of work has been done on tactile interaction of the whole robot arm with the environment. Bauer [22] conducted very practical and useful research on haptic exploration of the environment. The idea underlying the algorithm is to identify the free space, object location and object shape by several attempts made by the robot arm in order to pass through an obstacle. It should be noted, however, that the proposed system cannot detect the contact point coordinates, requires a time-consuming obstacle identification process and, as the authors reported, the exploration algorithm fails when several collisions occur simultaneously.

Substantially more research has been done in the field of object exploration and object recognition by the humanoid robot hand. Okamura *et al.* [23] introduced an approach for haptic exploration of an unknown object through traversing the object surface by robot fingers. The process consists of a sequence of phases, in which some fingers are responsible for grasping, and others roll and slide over the object surface. Exploratory strategies for the determination of the object geometry with haptic sensing have been developed [24, 25]. Instead of mounting a distributed tactile sensor on the finger link, the method described in Ref. [26] roughly detects a contact and then initiates the motion of the fingertip along the contour. An approach to real-time shape recognition and grasping of unknown objects by a robot hand with soft fingers and an omnidirectional camera is proposed in Ref. [2]. The polygon circumscribing the horizontal cross-section of the object is calculated using the volume intersection method.

However, the approaches mentioned above are mostly intended for grasping optimization, not for obstacle avoidance. To cope with the spatial uncertainty of an unknown, unstructured environment, we elaborated a novel concept of obstacle avoidance through physical interaction. When the robot arm is obstructed by an obstacle, the controller directs the manipulator to the target point in such a way that the robot arm surface follows the contour of the object. For object shape recognition, the method based on B-spline interpolation is proposed.

4.2. Algorithm of Obstacle Avoidance Through Tactile Sensing

The procedure of obstacle avoidance is as follows:

(i) The contact state is recognized once the actual torque in the robot joint exceeds the assigned threshold value.

(ii) The control system computes the normal force vector F_n based on measured joint torque values and the contact point detection algorithm.

(iii) Local admittance control generates compliant motion according to the applied normal force vector and maintains the contact force value to be nearly 1 N.

(iv) The object shape is approximated by the cubic B-spline. The next position of the robot arm is defined by the direction of the tangent vector to the curve at the contact point and the cross product of vectors locating the end-effector P_t and target point P_f (Fig. 18).

(v) If the value of cross product equals zero, the vectors P_t and P_f become collinear. That means that the robot end-effector has reached the target point.

Figure 18 graphically illustrates the obstacle avoidance procedure through haptic interaction. Point A presents the position of the end-effector when the contact state is detected. The robot arm moves to the target point B (the place where the object needs to be grasped is located), establishing continuously physical contact with the obstacle.

The methods for contact state recognition and computation of contact point coordinates are given below.

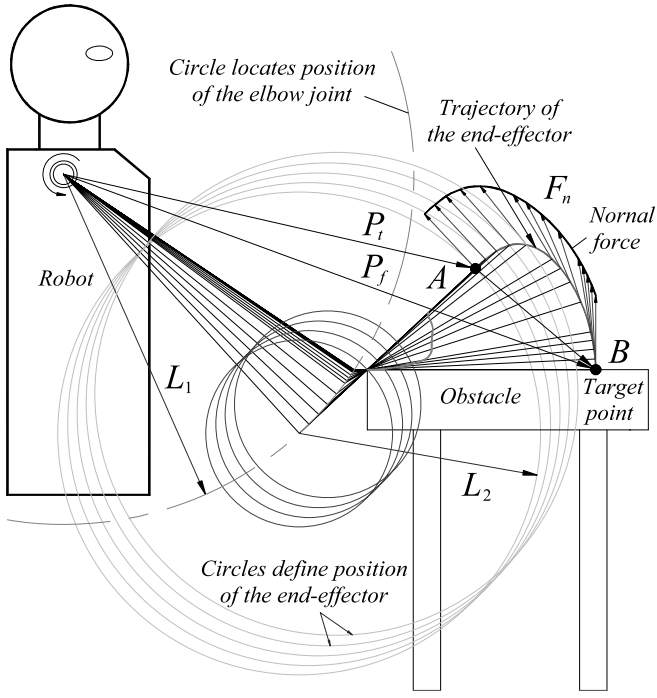

Figure 18. Layout of the obstacle avoidance procedure.

4.3. Contact State Recognition

During the first stage of control the robot links rotate until one of them contacts the object. In addition to contact force, torque sensors continuously measure the gravity and inertial load. Since the robot arm moves with low angular speed, the inertial load component can be disregarded. The Newton–Euler dynamics formulation was adopted to calculate the reference values of the gravity torques. The application of the algorithm for robot arm iSoRA results in the equation of the gravitational torque vector:

$$G(\theta) = \begin{bmatrix} \tau_{g1} \\ \tau_{g2} \\ \tau_{g3} \\ \tau_{g4} \end{bmatrix} = \begin{bmatrix} L_{M2}m_2(s_1c_2c_4 + c_1c_3s_4 + s_1s_2s_3s_4) + (L_{M1}m_1 + L_1m_2)s_1c_2 \\ L_{M2}m_2(c_1s_2c_4 - c_1c_2s_3s_4) + (L_{M1}m_1 + L_1m_2)c_1s_2 \\ L_{M2}m_2(-c_1s_2c_3s_4 - s_1s_3s_4) \\ L_{M2}m_2(-c_1s_2s_3c_4 + s_1c_3c_4 + c_1c_2s_4) \end{bmatrix} \begin{bmatrix} g \\ g \\ g \\ g \end{bmatrix}, \tag{15}$$

where τ_{gi} is the gravitational torque in the ith joint, m_1 and m_2 are the point masses of the first and second link, respectively, L_{M1} and L_{M2} are the distances from the first and second link origins to the centers of mass, respectively, L_1 is the upper arm length, and c_1, c_2, c_3, c_4, s_1, s_2, s_3 and s_4 are abbreviations for $\cos(\theta_1)$, $\cos(\theta_2)$, $\cos(\theta_3)$, $\cos(\theta_4)$, $\sin(\theta_1)$, $\sin(\theta_2)$, $\sin(\theta_3)$ and $\sin(\theta_4)$, respectively.

In the case when the robot arm performs planar motion in the X_0Z_0 plane, only the first and fourth joints operate. The gravity torques acting at the first τ_{g1} and fourth joints τ_{g4} are derived from:

$$\begin{aligned} \tau_{g1} &= m_2 g(L_{M2}\sin(\theta_1 + \theta_4) + L_1\sin(\theta_1)) + m_1 g L_{M1}\sin(\theta_1); \\ \tau_{g4} &= m_2 g L_{M4}\sin(\theta_1 + \theta_4). \end{aligned} \tag{16}$$

The experiment with the fourth joint of the robot arm was conducted in order to measure the gravity torque (Fig. 19a) and to estimate the error by comparison with a reference model (Fig. 19b).

As can be seen from Fig. 19b, the peak values of the gravity torque estimation error arise at the start and stop stages of the joint rotation. The reason for this is the high inertial loading that provokes the vibrations during acceleration and deceleration transients. This disturbance can be evaluated by using accelerometers and excluded from further consideration. Observing the measurement error plot, we can assign the relevant threshold that triggers control of the constraint motion.

4.4. Contact Point Determination

The information about the contact point coordinates is necessary for the calculation of the object stiffness, applied force vector and object shape reconstruction. The

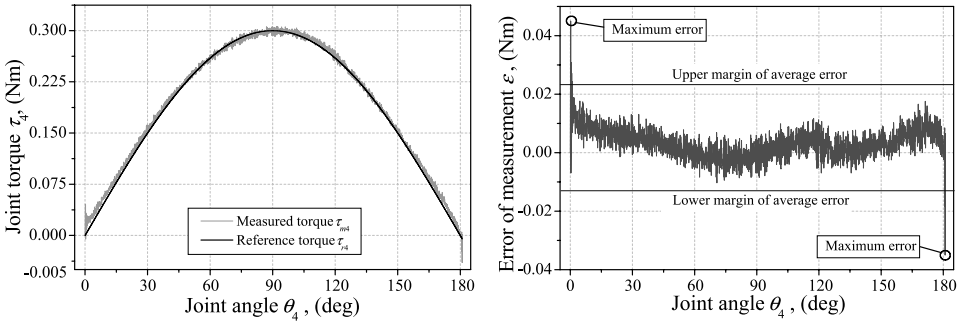

(a) (b)

Figure 19. Experimental results of gravity measurement.

tactile sensor can be useful in this case. However, our goal is to perform tactile interaction with the environment without any complicated sensory system of the robot. The method we present here results from the assumption that the coordinates of intersection of the subsequent profiles of the robot arm equal the coordinates of the contact points during tactile obstacle avoidance. This assumption holds true since the increment of joint angles is small enough because of the fast sampling rate of 1700 Hz and slow collision avoidance motion. Let us consider the case when the forearm is contacting with an object. The line representing the robot forearm is located by the following position vectors:

$$P_{\mathrm{t}} = \begin{bmatrix} P_{\mathrm{t}x} \\ P_{\mathrm{t}y} \\ P_{\mathrm{t}z} \end{bmatrix} = \begin{bmatrix} L_2(s_1s_2s_3s_4 + c_1c_3s_4 + s_1c_2c_4) + L_1s_1c_2 \\ -L_2(c_2s_3s_4 - s_2c_4) + L_1s_2 \\ -L_2(c_1s_2s_3s_4 - s_1c_3s_4 + c_1c_2c_4) - L_1c_1c_2 \end{bmatrix} \tag{17}$$

$$P_{\mathrm{e}} = \begin{bmatrix} P_{\mathrm{e}x} \\ P_{\mathrm{e}y} \\ P_{\mathrm{e}z} \end{bmatrix} = \begin{bmatrix} L_1s_1c_2 \\ L_1s_2 \\ -L_1c_1c_2 \end{bmatrix}, \tag{18}$$

where L_1 and L_2 are the lengths of the upper arm and forearm, respectively, and P_{t} and P_{e} are the vectors locating the tip of robot arm and elbow joint, respectively.

During surface following, the subsequent position of the link is defined by joint angle increments $\theta_i + \Delta\theta_i$. New coordinates of the end points of forearm $P_{\Delta\mathrm{t}}$ and $P_{\Delta\mathrm{e}}$ are derived through substitution $\theta_i + \Delta\theta_i$ into (17) and (18), respectively. The intersection point of two consequent lines defines the coordinates of the contact point. In the case of planar motion (when $\theta_2 = \theta_3 = 0$), the intersection coordinates $(P_{\mathrm{C}x}; P_{\mathrm{C}z})$ can be defined using determinants:

$$P_{\mathrm{C}x} = \frac{\begin{vmatrix} \begin{vmatrix} P_{\Delta\mathrm{e}x} & P_{\Delta\mathrm{e}z} \\ P_{\Delta\mathrm{t}x} & P_{\Delta\mathrm{t}z} \end{vmatrix} & P_{\Delta\mathrm{e}x} - P_{\Delta\mathrm{t}x} \\ \begin{vmatrix} P_{\mathrm{e}x} & P_{\mathrm{e}z} \\ P_{\mathrm{t}x} & P_{\mathrm{t}z} \end{vmatrix} & P_{\mathrm{e}x} - P_{\mathrm{t}x} \end{vmatrix}}{\begin{vmatrix} P_{\Delta\mathrm{e}x} - P_{\Delta\mathrm{t}x} & P_{\Delta\mathrm{e}z} - P_{\Delta\mathrm{t}z} \\ P_{\mathrm{e}x} - P_{\mathrm{t}x} & P_{\mathrm{e}z} - P_{\mathrm{t}z} \end{vmatrix}} = \frac{-L_1(s_{\Delta 14}s_4 - s_{14}s_{\Delta 4})}{s_{\Delta 1\Delta 4}} \tag{19}$$

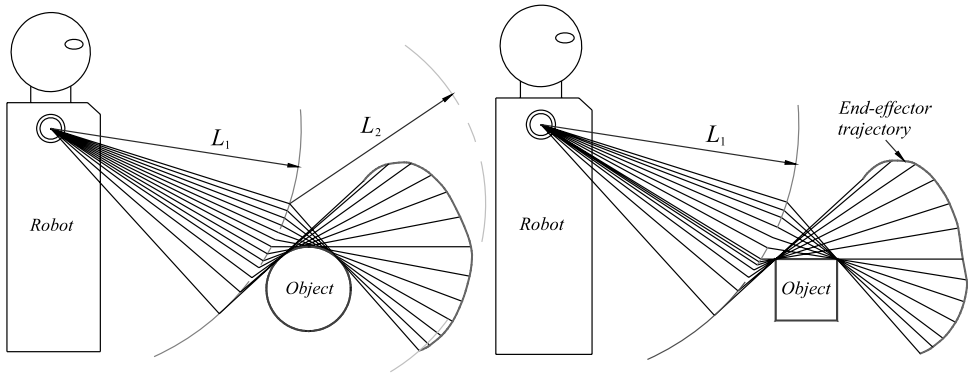

Figure 20. Shape recognition of the round and rectangular object.

$$P_{Cz} = \frac{\begin{vmatrix} \begin{vmatrix} P_{\Delta ex} & P_{\Delta ez} \\ P_{\Delta tx} & P_{\Delta tz} \end{vmatrix} & P_{\Delta ez} - P_{\Delta tz} \\ \begin{vmatrix} P_{ex} & P_{ez} \\ P_{tx} & P_{tz} \end{vmatrix} & P_{ez} - P_{tz} \end{vmatrix}}{\begin{vmatrix} P_{\Delta ex} - P_{\Delta tx} & P_{\Delta ez} - P_{\Delta tz} \\ P_{ex} - P_{tx} & P_{ez} - P_{tz} \end{vmatrix}} = \frac{-L_1(c_{14}s_{\Delta 4} - c_{\Delta 14}s_4)}{s_{\Delta 1 \Delta 4}}, \qquad (20)$$

where s_{14}, $s_{\Delta 14}$, $s_{\Delta 1 \Delta 4}$, $s_{\Delta 4}$, c_{14} and $c_{\Delta 14}$ stand for $\sin(\theta_1 + \theta_4)$, $\sin(\theta_1 + \Delta\theta_1 + \theta_4 + \Delta\theta_4)$, $\sin(\Delta\theta_1 + \Delta\theta_4)$, $\sin(\theta_4 + \Delta\theta_4)$, $\cos(\theta_1 + \theta_4)$ and $\cos(\theta_1 + \Delta\theta_1 + \theta_4 + \Delta\theta_4)$, respectively.

4.5. Shape Recognition

Studies on human tactile perception show that edge or contour following is one of the common exploratory procedures that people use for the determination of object geometry [27]. We propose the tactile object shape recognition method based on the acquisition and formulation of information as image primitives. Tactile images are generated when the robot arm registers a series of contact points with an object. The node points obtained by employing the contact point detection algorithm (17)–(20) are interpolated by B-splines. Thus, complex shapes of obstacles can be detected accurately. Graphical modeling of the shape recognition during avoidance of round and rectangular obstacle is shown in Fig. 20.

The B-spline curve is expressed as a convex combination of polygon vertex position vectors. The spline method solving the connection problem that exists with other techniques features superior controllability and desired continuity [28]. To obtain C^2 continuity, we employ a cubic uniform B-spline. The segment i of spline curve $P_i(t)$ is a cubic parametric polynomial described by:

$$P_i(t) = \frac{1}{6}[\,t^3 \quad t^2 \quad t \quad 1\,] \begin{bmatrix} -1 & 3 & -3 & 1 \\ 3 & -6 & 3 & 0 \\ -3 & 0 & 3 & 0 \\ 1 & 4 & 1 & 0 \end{bmatrix} \begin{bmatrix} P_{i-1} \\ P_i \\ P_{i+1} \\ P_{i+2} \end{bmatrix}, \qquad (21)$$

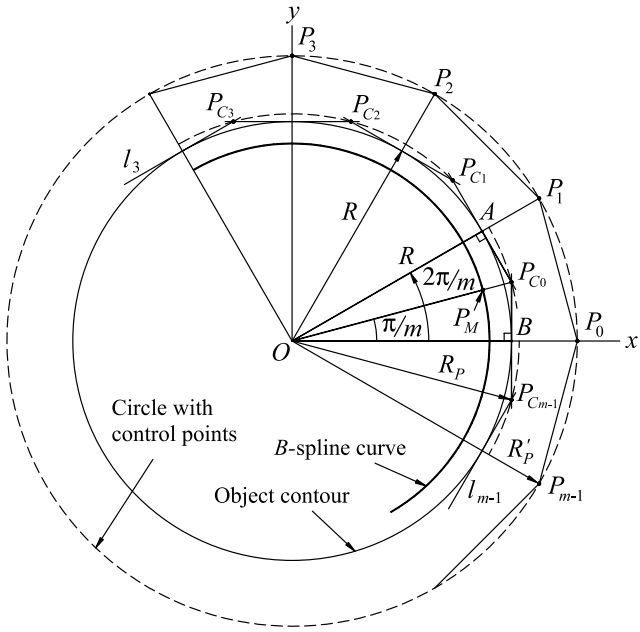

Figure 21. Method of object shape approximation.

where P_{i-1}, P_i, P_{i+1} and P_{i+2} are the control points (contact points preliminary calculated from (19) and (20)); $i = 1, 2, \ldots, n-2$; $n+1$ is the number of given control points; and $t \in [0, 1]$ is the global parameter.

An actual spline curve is made of these curve segments $P_i(t)$. Let us estimate the error of object shape approximation by using the proposed approach. We assume that the object has a circular contour of radius R and the contact points P_{Ci} defined by intersections of subsequent robot link positions l_i and l_{i+1} are equidistant (Fig. 21). The radius of circle R_P, which the contact point is placed on, is expressed from the right triangle ΔOAP_{C0}:

$$R_P = \frac{R}{\cos(\pi/m)}, \tag{22}$$

where m is the number of control points (equal to $n+1$).

The coordinates of contact points P_{Ci} are defined by:

$$\begin{aligned} P_{Ci} &= \left(R_P \cos\left(\frac{2\pi i}{m} - \frac{\pi}{m}\right), R_P \sin\left(\frac{2\pi i}{m} - \frac{\pi}{m}\right)\right) \\ &= \left(\frac{R\cos(\frac{2\pi i}{m} - \frac{\pi}{m})}{\cos(\pi/m)}, \frac{R\sin(\frac{2\pi i}{m} - \frac{\pi}{m})}{\cos(\pi/m)}\right). \end{aligned} \tag{23}$$

For the sake of simplification of further computations, we assume the radius R of one unit and rotate the contact points P_{Ci} in the clockwise direction on angle π/m. The transformed control points P_i are placed on the circle with a different graphical

scale for geometrical visualization (numerical value of R'_{P} is equal to R_{P}). Cartesian coordinates of control points can be calculated from:

$$P_i = \left(\frac{\cos(\frac{2\pi i}{m})}{\cos(\pi/m)}, \frac{\sin(\frac{2\pi i}{m})}{\cos(\pi/m)} \right), \tag{24}$$

where $i = 0, 1, \ldots, m-1$.

The worst approximation is obtained midway between the control points, i.e., $P_i(0.5)$. The midpoint of a cubic segment, however, is easily derived from (21) as:

$$P_{\mathrm{M}} = P_1(0.5) = \frac{1}{48}(P_{m-1} + 23P_0 + 23P_1 + P_2). \tag{25}$$

After substitution of the control point coordinates from (24) to (25) we have:

$$P_{\mathrm{M}} = \left(\frac{(1+\cos\theta)(11+\cos\theta)}{24\cos(\theta/2)}, \frac{\sin\theta(11+\cos\theta)}{24\cos(\theta/2)} \right), \tag{26}$$

where $\theta = 2\pi/m$.

The deviation E (%) from a true circle is expressed as:

$$E = \left(1 - \sqrt{P_{\mathrm{M}}^2}\right) \times 100 = \frac{1-\cos(2\pi/m)}{12} \times 100. \tag{27}$$

The deviations from a true circle for different numbers of control points are listed in Table 1.

The proposed approach based on the B-spline can, therefore, provide an excellent approximation to a circle. Since the robot angular iterations are fairly small, the number of control points is huge, which results in a very precise contour recognition. The curvature of the curve segment i is calculated as:

$$P_i = \frac{P'_{ix} P''_{iy} - P'_{iy} P''_{ix}}{(P'^2_{ix} + P'^2_{iy})^{3/2}}. \tag{28}$$

The algorithm of contour recognition of the rectangular-shaped object is as follows. In the presence of a vertex, the lines intersect in one point. When the coordinates of the intersection point change drastically, the subsequent vertex is recognized. The line connecting two vertices define the edge of the object (Fig. 20). More complicated shapes can be detected by a combination of B-spline interpolation, vertex and edges recognition. If the curve-defining vectors P_{i-1}, P_i, P_{i+1} and

Table 1.
Deviation from a true circle

	m								
	12	16	20	24	28	32	36	40	44
E (%)	1.117	0.634	0.408	0.284	0.209	0.16	0.127	0.103	0.085

P_{i+2} lie collinear, the curve segment defined by those four position vectors degenerates to a line segment. This line segment connects continuously to the neighboring curve segments with continuity up to the curvature vector. This feature is extremely useful in the case of complex shape recognition.

4.6. Estimation of Contacting Object Stiffness

During the first stage of control the robot links rotate until one of them contacts the object. The control system detects the contact state using the reference and actual torque values in the joints.

During contact transition we can acquire information about the collision danger of contacting the object through its stiffness estimation and represent this information to the operator. This can be done by establishing stiff contact through PD control of the robot arm with high P-gain until the joint torque exceeds the threshold value of 0.05 Nm. The robot was commanded to follow the trajectory in free space with a constant angular velocity. An object was placed on this path so that the second link would contact it. The joint torque was recorded for the fourth joint while contacting with object. Figure 22a–e shows experimental results when the link comes into contact with objects having different stiffness varying from a very low rate to a very high, i.e., a piece of sponge, rubber sponge, rubber, chemical wood and aluminum, respectively. The time derivative of the torque during impact is given in Fig. 22f.

It is apparent from the plots presented in Fig. 22 that the stiffer the contacting object, the smaller the angle of robot joint rotation. The elastic deformation of the object and inherent compliance of robot joints lead to rotation of the robot arm by angle $\Delta\theta_i$ during contact transience (Fig. 23).

The proposed method of estimation of contacting object stiffness is based on the principles of solid mechanics for an elastic linear material model. It includes the following stages: (i) calculation of the total elastic deformation of robot link with object δ_i, (ii) estimation of the total stiffness of a robot link–object pair k_i, and (iii) computation of the object stiffness k_o from the given values of the robot link stiffness and total stiffness. The given data are contact point coordinates P_{Ci} (derived from (19) and (20)), the changes in joint angle $\Delta\theta_i$ and joint torque value $\Delta\tau_i$ while colliding ($\Delta\theta_i$ and $\Delta\tau_i$ are derived from Fig. 22).

The distance that contact point C on the robot link surface 1 moves perpendicularly to the radius r_i under torque $\Delta\tau_i$, is equal to $r_i\Delta\theta_i$ (since the angle $\Delta\theta_i$ is fairly small). The unknown angle φ_i can be found by taking into account that $\angle C'CB = \angle OCA = \varphi_i$:

$$\varphi_i = \arctan\left(\frac{OA}{CA}\right) = \arctan\left(\frac{h_i}{P_{C_i}}\right), \tag{29}$$

where h_i equals half of the robot link thickness.

The total elastic deformation is calculated from the right triangle $\Delta CBC'$ as:

$$\delta_i = \Delta\theta_i r_i \cos(\varphi_i). \tag{30}$$

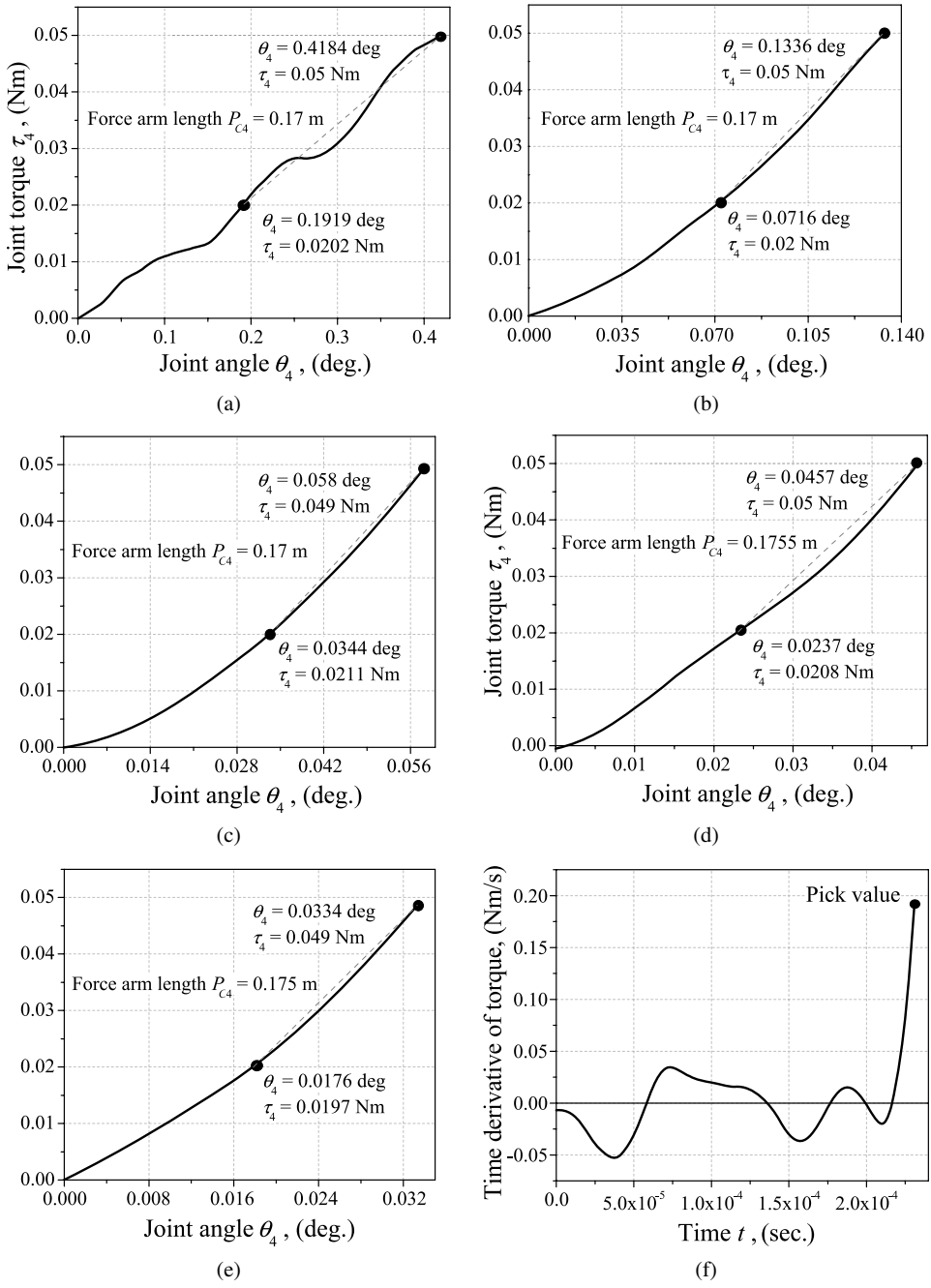

Figure 22. Experimental results of stiffness estimation.

The radius of the contact point trajectory r_i is found as $r_i = \sqrt{P_{C_i}^2 + h_i^2}$ through consideration of the right triangle ΔCAO.

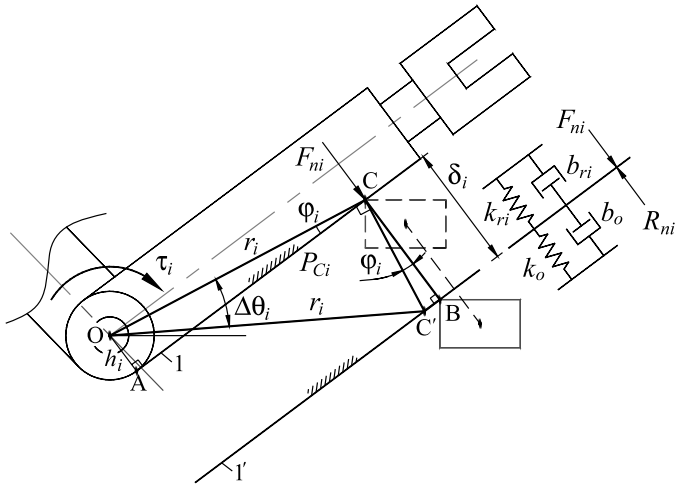

Figure 23. Scheme for elastic deformation calculation.

Table 2.
Findings from the experimental diagrams

Parameter	Sponge	Rubber sponge	Rubber	Wood
$\Delta\theta_i 10^{-4}$ (rad)	39.53	10.82	4.12	3.84
$\Delta\tau_i 10^{-2}$ (Nm)	2.98	3.0	2.79	2.92

Now, we can easily calculate the total stiffness:

$$k_i = \frac{F_{\mathrm{n}i}}{\delta_i} = \frac{\Delta\tau_i}{P_{\mathrm{C}_i}\Delta\theta_i r_i \cos(\varphi_i)} = \frac{\Delta\tau_i}{P_{\mathrm{C}_i}\Delta\theta_i\sqrt{P_{\mathrm{C}_i}^2 + h_i^2}\cos(\arctan(h_i/P_{\mathrm{C}_i}))}. \quad (31)$$

By linear approximation, we take into account only two values of θ_i for τ_i nearest to 0.02 and 0.05 Nm. Then, from the experimental diagrams (Fig. 22a–e) we obtain $\Delta\theta_i$, and $\Delta\tau_i$ and list them in Table 2.

The total elastic deformation δ_i is made up of elastic deformation caused by object compliance δ_{o} and that generated by joint flexibility $\delta_{\mathrm{r}i}$. That is, we can write:

$$\delta_i = \frac{F_{\mathrm{n}i}}{k_i} = \delta_{\mathrm{o}} + \delta_{\mathrm{r}i} = \frac{R_{\mathrm{n}i}}{k_{\mathrm{o}}} + \frac{F_{\mathrm{n}i}}{k_{\mathrm{r}i}}, \quad (32)$$

where $R_{\mathrm{n}i}$ is the reaction, the absolute value of which equals $F_{\mathrm{n}i}$; k_{o} and $k_{\mathrm{r}i}$ are the stiffness of the object and the stiffness of the robot link, respectively.

The coefficient $k_{\mathrm{r}i}$ is mainly defined by torque sensor stiffness, harmonic drive stiffness, structural flexibility and P-gain magnitude. Detailed examination has showed that a complex theoretical model of robot link stiffness can hardly provide accurate estimation of $k_{\mathrm{r}i}$. Therefore, we can set the value of robot link stiffness

Table 3.
Total stiffness and object stiffness

Parameter	Sponge	Rubber sponge	Rubber	Wood
k_i (N/m)	260.84	959.3	2343.78	2469.04
k_o (N/m)	282.04	1325.92	7223.94	8562.90

close to the total stiffness in the hardest contact case. This assumption is valid because during impact with a hard environment, such as the aluminum plate, the contact deformation of the object is too small to be accounted for ($k_o \approx \infty$). Thus, using (29)–(31) and the data presented in Fig. 22a–e we derive the unknown value of k_{ri}:

$$k_{ri} = \frac{0.0293 \text{ Nm}}{0.175 \cdot 2.758 \cdot 10^{-4} \cdot 0.1776 \cdot 0.986 \text{ m}^2} = 3468.6 \frac{\text{N}}{\text{m}}.$$

The stiffness of the objects is calculated from:

$$k_o = \frac{k_{ri} \cdot k_i}{k_{ri} - k_i}, \tag{33}$$

where k_i is defined by (31). Derived values of the total stiffness k_i and object stiffness k_o are given in Table 3.

The obtained results demonstrate a strong correspondence of correlation among the calculated object stiffness with that of real objects. Naturally, the actual stiffness of the colliding environment differs from the calculated one with finite error. To achieve high accuracy, specific equipment is needed. However, our aim was only assessment of the danger level of robot arm collision with an object. Specifically, we can define that sponge and rubber sponge material are safe for interaction, but rubber, wood and metal pose a threat while striking the robot arm. Consequently, we have succeeded in solving the main task — object classification by getting information about stiffness during impact.

In the case when the collision must be detected robustly without consideration of object properties, the value of the time derivative of torque can be used to judge the impact value (Fig. 22f).

4.7. Experimental Results of Obstacle Avoidance Through Haptic Interaction and Accomplishment of Human Motion Following

The still images of the robot arm motion video are given in Fig. 24.

The robot arm is controlled by the program on a Dell Precision computer (CPU: Intel Pentium, 3.2 GHz, memory 2 GB). The results show that the robot arm slides over the obstacle surface (black object on the table) smoothly and maintains constant physical contact with it till the end-effector reaches the target point. The speed of the obstacle avoidance can be adjusted online depending on the object properties

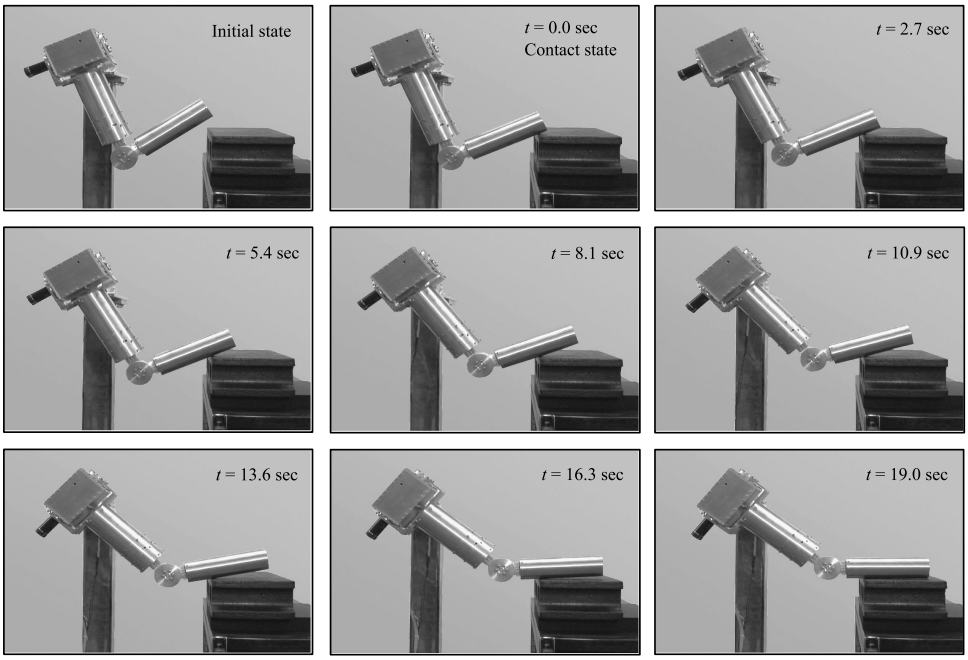

Figure 24. Experiment of obstacle avoidance through whole-arm tactile interaction.

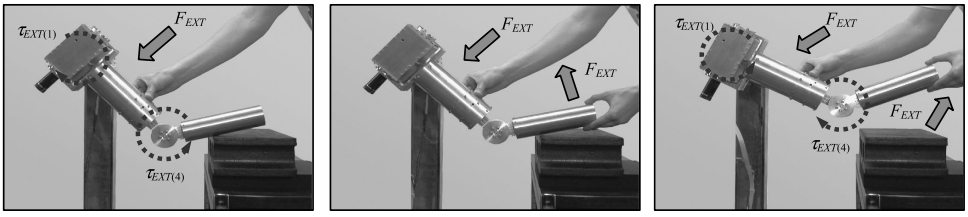

Figure 25. Experiment of human-following motion.

and shape. For example, a shape composed of edges and vertices can be handled faster than one with curve contour.

The remarkable opportunity of ensuring safe robot–environment interaction is that we can establish different dynamic parameters of the robot arm contacting with the environment according to the calculated object stiffness (by using the method described in Section 4.6). This is an inherent capability of humans, since when we collide with stiff objects we tend to soften our muscles as much as we can.

In order to verify the ability of the developed robot arm iSoRA to safely interact with human beings along the entire surface and to perform cooperative tasks through human-following motion, the experiment was conducted. In the first stage of interaction, force was applied to the upper arm of the humanoid robot arm. The robot arm generates compliant motion according to the applied force value and comes to the position shown in Fig. 25 (left). Then, an additional force was applied

to the forearm of iSoRA. Since the net torque has a counter-clockwise direction at the pitch joint of the shoulder, the robot arm generates continuous compliant motion upward (Fig. 25, right).

It can be seen from Fig. 25 that the elaborated intelligent joint admittance control enables the human cooperating with the service robot to control the position and orientation of the robot arm through haptic interaction along the entire robot arm surface. The robot successfully recognizes the human-following task and generates compliant motion in a safe manner.

4.8. Application of a Robot with a Tactile-Sensitive Robot Arm

The proposed concept opens a wide range of potential applications in service robotics and teleoperation. Here, we discuss other possible applications of the robot arm with whole-arm tactile sensing ability.

The obstacle avoidance presents significant issues for urban search and rescue robots. Such robots aim at assisting rescue workers in the investigation of unreachable areas, such as small cracks and pipes, or unsafe places by delivering visual information from cameras at the end-effector. Controllable compliance of the robot arm joint can be extremely useful in this application, since it provides whole-arm tactile interaction with the environment. Therefore, such type of manipulator has significant capabilities for performance improvement in comparison with conventional manipulators in the field of obstacle avoidance. We summarize possible cases of application of the robot enabling intelligent tactile obstacle avoidance as follows:

(i) A robot arm finds the path through interaction with obstacles in extremely cramped environments (Fig. 18).

(ii) A robot reaches for a visible object located inside a narrow space. The robot arm contacts and follows the surface of the obstacle represented by the sides of the box to fulfill the task (Fig. 26).

(iii) A robot reaches for an object located beyond the robot camera visibility range. In such cases the robot arm needs to be equipped with additional cameras in order to process the collision softly on its own (Fig. 27).

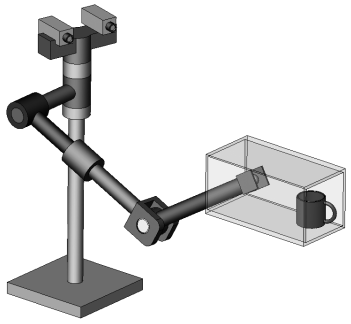

Figure 26. Robot reaches the object located in narrow space.

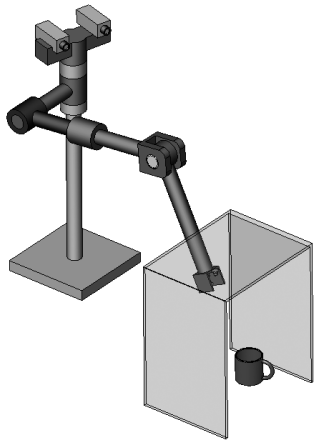

Figure 27. Robot reaches the object located beyond visibility range.

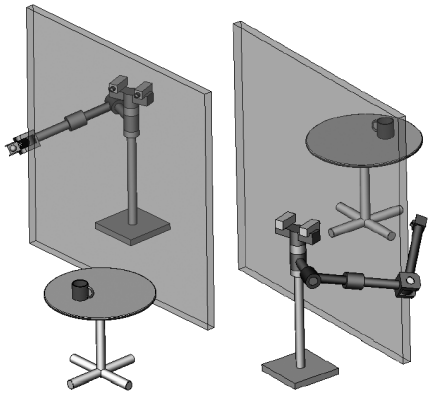

Figure 28. Robot investigates the indoor environment.

(iv) A robot investigates the indoor area to achieve situational awareness without the necessity of its bulky body entering the room. When the situation is assessed, the robot body can elude the jamb and enter into the room carefully (Fig. 28).

(v) A robot structures the environment. A vision system of conventional robots cannot determine the distance to the object in three-dimensional space. By tactile interaction, the robot can precisely define the object location and reachable working area.

The developed robot and proposed algorithms can enable a service robot not only to work in a dynamic unstructured environment, but also to cooperate with humans in a safe manner and to assist rescue workers in the investigation of unreachable places.

5. Conclusions and Future Work

A new whole-sensitive robot arm, iSoRA, was developed to provide human-like capabilities of performing contact tasks in a broad variety of environments. Each joint was facilitated with a high-performance optical torque sensor. Intelligent variable admittance control and reflex action-based impact control were elaborated to realize safe, smooth and natural human–robot interaction. We introduced the exponential functional dependency between the sensed force and stiffness to impart human-like damping and stiffness behavior to the robot arm. Experimental results of impact revealed that large contact forces, mainly used as criteria of collisions, do not indicate the impact state, while the time derivative of the force value does. The magnitude of time derivative of torque was used as an indicator of the collision state. To realize reflexive human-like behavior, the stiffness of the impedance model of the robot arm was reduced drastically during the collision transient. This was achieved by means of the reciprocal functional dependency of stiffness on the value of the time derivative of the torque. The effectiveness of the controllers was experimentally illustrated on the whole-sensitive robot arm. The conventionally impedance-controlled robot can provide contacting task only at the tip of the end-effector with predetermined dynamics. By contrast, approaches developed by us provide delicate continuous safe interaction of all surface of the robot arm with the environment.

The proposed concept of obstacle avoidance through whole-arm tactile interaction enables the manipulator to adapt the planned motion to the obstacle shape. Such an algorithm is especially valuable for service robots working in real indoor environments. Tactile interaction gains the essential information about the contacting object (shape, stiffness, location, etc.). Numerical simulation revealed that the described method for object shape recognition based on the B-spline approximation provides high accuracy of contour approximation. The method of object stiffness estimation is presented and verified. The experimental results presented show the validity and robustness of the proposed concept. Our approach can also be extended for object shape recognition and motion planning in three-dimensional space.

The subject of ongoing work is to adapt the dynamic parameters of the robot to the surface properties (stiffness, friction coefficient) of the contacting object. Object mobility and object fixation will be examined by observing the external force pattern during physical interaction.

Acknowledgements

The research is supported in part by a Japan Society for the Promotion of Science Postdoctoral Fellowship for Foreign Scholars.

References

1. T. Lozano-Perez, A simple motion-planning algorithm for general robot manipulators, *IEEE J. Robotics Automat*. **3**, 224–238 (1987).

2. T. Yoshikawa, M. Koeda and H. Fujimoto, Shape recognition and grasping by robotic hands with soft fingers and omnidirectional camera, in: *Proc. IEEE Int. Conf. on Robotics and Automation*, Pasadena, CA, pp. 299–304 (2008).
3. V. J. Lumelsky, M. S. Shur and S. Wagner, Sensitive skin, *IEEE Sensors J.* **1**, 41–51 (2001).
4. V. Lumelsky and E. Cheung, Towards safe real-time robot teleoperation: automatic whole-sensitive arm collision avoidance frees the operator for global control, in: *Proc. IEEE Int. Conf. on Robotics and Automation*, Sacramento, pp. 797–802 (1991).
5. J. T. Feddema and J. L. Novak, Whole arm obstacle avoidance for teleoperated robot, in: *Proc. IEEE Int. Conf. on Robotics and Automation*, San Diego, CA, pp. 3303–3309 (1994).
6. S. Morikawa, T. Senoo, A. Namiki and M. Ishikawa, Real-time collision avoidance using a robot manipulator with light-weight small high-speed vision system, in: *Proc. IEEE Int. Conf. on Robotics and Automation*, Rome, pp. 794–799 (2007).
7. F. Caccavael, C. Natale, B. Siciliano and L. Villani, Six-DOF impedance control based on angle/axis representation, *IEEE Trans. Robotics Automat.* **15**, 289–300 (1999).
8. H. Iwata, S. Kobashi, T. Aono and S. Sugano, Design of anthropomorphic 4-DOF tactile interaction manipulator with passive joints, in: *Proc. IEEE/RSJ Int. Conf. on Intelligent Robots and Systems*, Edmonton, pp. 1785–1790 (2005).
9. A. Bicchi and G. Tonietti, Fast and soft arm tactics: dealing with the safety-performance trade-off in robot arms design and control, *IEEE Robotics Automat. Mag.* **11**, 22–33 (2004).
10. G. Hirzinger, A. Albu-Schaffer, M. Hahnle, I. Schaefer and N. Sporer, On a new generation of torque controlled light-weight robots, in: *Proc. IEEE Int. Conf. on Robotics and Automation*, Seoul, pp. 3356–3363 (2001).
11. N. Mitsunaga, T. Miyashita, H. Ishiguro, K. Kogure and N. Hagita, Robovie IV: a communication robot interacting with people daily in an office, in: *Proc. IEEE/RSJ Int. Conf. Intelligent Robots and Systems*, Beijing, pp. 5066–5072 (2006).
12. D. Tsetserukou, R. Tadakuma, H. Kajimoto and S. Tachi, Optical torque sensors for local impedance control realization of an anthropomorphic robot arm, *J. Robotics Mechatron.* **18**, 121–130 (2006).
13. D. Tsetserukou and S. Tachi, Torque sensors for robot joint control, in: *Sensors, Focus on Tactile, Force and Stress Sensors*, J. G. Rocha and S. Lanceros-Mendes (Eds), pp. 15–36. Austria (2008).
14. N. Hogan, Impedance control: an approach to manipulation, Part I–III, *ASME J. of Dyn. Syst. Meas. Control*. **107**, 1–23 (1985).
15. R. Carelli and R. Kelly, Adaptive impedance/force controller for robot manipulators, *IEEE Trans. Automatic Control*. **36**, 967–972 (1991).
16. R. V. Dubey, T. F. Chang and S. E. Everett, Variable damping impedance control of a bilateral telerobotic system, *IEEE Control Syst. Mag.* **17**, 37–44 (1997).
17. T. Tsumugiwa, R. Yokogawa and K. Hara, Variable impedance control based on estimation of human arm stiffness for human–robot cooperative calligraphic task, in: *Proc. IEEE Int. Conf. Robotics and Automation*, Washington, DC, pp. 644–650 (2002).
18. D. P. Ferris and C. T. Farley, Interaction of leg stiffness and surface stiffness during human hopping, *J. Appl. Physiol*. **82**, 15–22 (1997).
19. M. M. Rahman, R. Ikeura and K. Muzutani, Investigating the impedance characteristics of human arm for development of robot to cooperate with human operators, in: *Proc. IEEE Int. Conf. on Systems, Man and Cybernetics*, Tokyo, pp. 676–681 (1999).
20. I. D. Walker, Impact configuration and measures for kinematically redundant and multiple armed robot system, *IEEE Trans. Robotics Automat*. **10**, 670–683 (1994).

21. R. Volpe and P. Khosla, A theoretical and experimental investigation of impact control for manipulators, *Int. J. Robotics Res*. **12**, 351–365 (1993).
22. J. Bauer, Mobile robot with tactile arm used for exploration and pushing tasks, in: *Proc. IEEE/RSJ Int. Conf. on Intelligent Robots and Systems*, Osaka, pp. 560–567 (1996).
23. A. M. Okamura, M. L. Turner and M. R. Cutkosky, Haptic exploration of objects with rolling and sliding, in: *Proc. IEEE Int. Conf. on Robotics and Automation*, Albuquerque, pp. 2485–2490 (1997).
24. S. Caselli, C. Magnaninni, F. Zanichelli and E. Caraffi, Efficient exploration and recognition of convex objects based on haptic perception, in: *Proc. IEEE Int. Conf. on Robotics and Automation*, Minneapolis, MN, pp. 3508–3515 (1996).
25. A. S. Rao and K. Y. Goldberg, Shape from diameter: recognizing polygonal parts with a parallel-jaw gripper, *Int. J. Robotics Res.* **13**, 16–37 (1994).
26. M. Kaneko, H. Maekawa and K. Tanie, Active tactile sensing by robotic fingers based on minimum-external-sensor-realization, in: *Proc. IEEE Int. Conf. on Robotics and Automation*, Nice, pp. 1289–1294 (1992).
27. R. L. Klatzky and S. Lederman, Intelligent exploration by the human hand, in: *Dexterous Robot Manipulation*, S. T. Venkataraman and T. Iberall (Eds), pp. 66–81. Springer, New York, NY (1990).
28. F. Yamaguchi, *Curves and Surfaces in Computer Aided Geometric Design*. Springer-Verlag, Berlin (1988).

About the Authors

Dzmitry Tsetserukou received the BS degree with honors in Electrical Engineering from the Mogilev Machine Building Institute, Belarus, in 1999, the MS degree in Mechanical Engineering from the National Academy of Sciences of Belarus, in 2002, and the PhD degree in Information Science and Technology from the University of Tokyo, Japan, in 2007. From 2002 to 2004, he was a Research Associate in the scientific research group at the National Academy of Sciences of Belarus. He is currently a JSPS Post-Doctoral Fellow in the Department of Information Physics and Computing at the University of Tokyo, Japan. He is a member of the IEEE and the author of over 50 technical publications, three patents, a book chapter and a book. His research interests include humanoid robots, force/torque sensors, impedance and admittance control, teleoperation, haptic interfaces and displays, and affective haptics.

Naoki Kawakami received the MS and PhD degrees from the University of Tokyo, Japan, in 1996 and 1999, respectively. He is currently a Lecturer in the Department of Information Physics and Computing at the University of Tokyo. His research interests include virtual reality, real-time remote robotics, telexistence and retro-reflective projection technology. He is the author of over 150 technical publications.

Susumu Tachi received his BS, MS and PhD degrees from the University of Tokyo, in 1968, 1970 and 1973, respectively. From 1975 to 1989, he was a Director of the Biorobotics Division at the Mechanical Engineering Laboratory, Ministry of International Trade and Industry, Tsukuba Science City, Japan. From 1989 to 2009, he was a Professor in the Department of Information Physics and Computing, University of Tokyo. He is currently a Professor in the Graduate School of Media Design, Keio University, Japan. He is a Founding Director of the Robotic Society of Japan and a Founding President of the Virtual Reality Society of Japan. From 1988, he has served as a Chairman of the IMEKO (International Measurement Confederation) Technical Committee on Measurement in Robotics. He is a member of IEEE VR Steering Committee, and has served as a General Chair of IEEE VR 2001 and 2002. He was responsible for the following research projects: Guide Dog Robot (1976–1983), National Large Scale Project on Advanced Robotics in Hazardous Environment (1983–1990), National Large Scale Project on Humanoids and Human Friendly Robotics (1998–2003), and CREST Project on Telexistence Communication Systems (2000–2005). He is the author of over 500 technical publications. His research interests include virtual reality, real-time remote robotics, telexistence and retro-reflective projection technology.